Chemical Science

EDGE ARTICLE

View Article Online
View Journal | View Issue

Cite this: *Chem. Sci.*, 2015, **6**, 5016

A smart all-in-one theranostic platform for CT imaging guided tumor microwave thermotherapy based on IL@ZrO_2 nanoparticles†

Haitang Shi,‡[ab] Meng Niu,‡[c] Longfei Tan,‡[a] Tianlong Liu,[a] Haibo Shao,[c] Changhui Fu,[a] Xiangling Ren,[a] Tengchuang Ma,[c] Jun Ren,[a] Linlin Li,[a] Huiyu Liu,[a] Ke Xu,*[c] Jianxin Wang,[d] Fangqiong Tang[a] and Xianwei Meng*[a]

Received 4th March 2015
Accepted 27th May 2015

DOI: 10.1039/c5sc00781j

www.rsc.org/chemicalscience

This study develops a simple hollow ZrO_2 nanostructure as a carrier to encapsulate ionic liquid (IL), which integrates the CT imaging function of the ZrO_2 shell and the microwave susceptibility function of the IL core. The simple nanostructure can be used as a multifunctional theranostic agent *via* combining diagnostic and therapeutic modalities into one "package". Based on the microwave susceptibility properties, the tumor inhibiting ratio can be over 90% in mice models after one-time thermal therapy upon microwave irradiation. *In vitro* and *in vivo* imaging results prove the potential of CT imaging application for real-time monitoring of biodistribution and metabolic processes, and assessing therapeutic outcomes. To our best knowledge, our study is the first example to achieve CT imaging and microwave thermal therapy simultaneously through a simple nanostructure. We anticipate that the simple IL@ZrO_2 nanostructure may build a useful platform for the clinical imaging guided therapy of tumors.

Introduction

The combination of diagnostic and therapeutic modalities into one "package", namely theranostics, opens up the possibility of revolutionizing techniques for survival of cancer.[1–4] This versatile technique provides an arsenal of various clinically relevant functions, which achieve excellent cancer control with minimal side effects by mixing and matching of these functions.[5] Therefore, research of theranostic agents for imaging guided therapy has aroused great interest in cancer research.[6–8] Multifunctional nanoparticles are one of the most promising options for clinical theranostic agents.[9–11] Many nanocomposites with anticancer and imaging functions have been designed and created.[12–14] In these tumor theranostic agents, the diagnostic modalities include one or more imaging techniques, such as X-ray computed tomography (CT) imaging,[9,15–17] magnetic resonance imaging,[5–7] positron emission tomography imaging,[18,19] photoacoustic imaging,[3,20,21] ultrasound imaging,[2,4] and upconversion luminescent imaging.[8,22,23] Among these techniques, CT imaging shows significant advantages in high image resolution ratio, accurate diagnosis results and high diagnosis efficiency. We found enhanced CT imaging properties of ZrO_2 for the first time based on the high atomic number and atomic mass of Zr. Thus, ZrO_2 nanoparticles will be desirable drug loading and delivery vesicles with an extra CT imaging property.

On the therapeutic side, chemotherapy,[24,25] nucleic acid delivery,[26,27] photodynamic,[1,8,28,29] photothermal ablation,[6,21,30,31] and radiation therapy[9,10,32] are included. The microwave thermotherapy technique is attracting research interest currently, due to the intuitive advantages of a non-intrusive heating model, fair depth of penetration in tissues and ideal potential for killing tumor cells without surgical risks or toxicity of chemotherapy. In previous works, microcapsules have been developed as microwave susceptible agents for tumor microwave thermal therapy *in vivo*,[33,34] but their micron size and single therapeutic function limit the clinical application of the microcapsules. Innovative theranostics are urgently needed that integrate a highly efficient microwave susceptible agent with an imaging modality.

Herein, we develop a multifunctional theranostic agent through a simple nanostructure of ionic liquid@ZrO_2 (IL@ZrO_2). The novel nanostructure integrates the CT imaging properties of hollow ZrO_2 nanoparticles and the high microwave heating efficiency of IL.[35] It shows powerful tumor inhibition rate (>90%) in mice models under a very low microwave irradiation of 1.8 W. A SD rat model is employed to prove the CT imaging properties for the real-time assessment of therapeutic outcomes visually, and a mini swine model is used to monitor

---

[a] *Laboratory of Controllable Preparation and Application of Nanomaterials, Center for Micro/nanomaterials and Technology, Technical Institute of Physics and Chemistry, Chinese Academy of Sciences, Beijing 100190, People's Republic of China. E-mail: mengxw@mail.ipc.ac.cn; Fax: +86-10-62554670; Tel: +86-10-82543521*

[b] *University of Chinese Academy of Sciences, Beijing 100049, People's Republic of China*

[c] *Department of Radiology, First Hospital of China Medical University, Shenyang 110001, People's Republic of China. E-mail: kexu@vip.sina.com*

[d] *Beijing M&Y Electronics Co. Ltd, Beijing 100015, People's Republic of China*

† Electronic supplementary information (ESI) available. See DOI: 10.1039/c5sc00781j

‡ These authors contributed equally to this work.

the biodistribution or metabolic processes visually in real-time without sacrificing batches of experimental animals at different time points after injection, as reported in previous literature.[36–38] The IL@ZrO_2 nanoparticles provide a smart 'all-in-one' theranostic platform and move new theranostic agents closer to clinical tumor treatment.

Results and discussion

Scheme 1 shows the synthesis procedure of hollow ZrO_2 nanoparticles *via* the template method and the encapsulation procedure of IL *via* the physical forced penetration method. The obtained IL@ZrO_2 nanoparticles possess CT imaging properties and microwave susceptibility properties simultaneously (Scheme 1a). Combined with the nano-sized morphology, the nanoparticles can be injected *via* intravenous injection and applied in CT imaging guided microwave thermal therapy *in vivo*. Due to the enrichment of IL@ZrO_2 in the tumor region, the nanoparticles can be applied for real-time monitoring of the therapeutic outcomes visually (Scheme 1b).

Characterization of the physicochemical properties of the multifunctional IL@ZrO_2 nanoparticles

Fig. 1a–c show the morphology and size distribution of the IL@ZrO_2 nanoparticles, with a regular spherical shape, narrow size distribution and good dispersion. The statistical average diameter is 345 nm, based on the histogram of the distribution of diameters in Fig. 1c. The thickness of the shell is ∼50 nm (Fig. 1a and b), which is suitable for inhibiting the infiltration of ionic liquid. The incomplete nanospheres in the SEM image (inset of Fig. 1a) and the TEM image (Fig. 1b) show the hollow structure clearly, providing a carrier for ionic liquid.

The composition of the hollow ZrO_2 nanoparticles and multifunctional IL@ZrO_2 nanoparticles was analyzed *via* energy dispersive X-ray analysis (EDX). Fig. 1d shows the formation of ZrO_2 nanoparticles with the presence of Zr and O and some additional Si, which may come from the SiO_2 template. C, F and P can be detected in Fig. 1e when the IL 1-butyl-3-methylimidazolium hexafluorophosphate ([Bmim]PF_6) is encapsulated in the hollow ZrO_2. This result provides powerful evidence for the successful encapsulation of [Bmim]PF_6. FT-IR spectra further confirm the combination of [Bmim]PF_6 and ZrO_2. Compared with the spectra of hollow ZrO_2 nanoparticles and neat [Bmim]PF_6, the spectrum of the multifunctional IL@ZrO_2 nanoparticles shows the typical characteristic peaks of [Bmim]PF_6 and ZrO_2 (Fig. 1f). Significantly, the characteristic peaks at 3217 and 3125 cm^{-1} are attributed to the stretching vibration of C–H in the imidazole ring. The two characteristic peaks at 3000–2700 cm^{-1} are assigned to the stretching vibration of saturated C–H bonds. The strong peak at 1169 cm^{-1} is owing to the stretching vibration of the imidazole ring and the peaks below 1000 cm^{-1} can be assigned to the bending vibration of C–H. The characteristic absorption peak of the P–F bond at 840 cm^{-1} can also be clearly observed. These results confirm the obtaining of multifunctional IL@ZrO_2 nanoparticles.

Fig. 1g–j show the high-angle annular dark-field scanning TEM (HAADF-STEM)-energy-dispersive X-ray (EDX) images of IL@ZrO_2, indicating the distribution of C and Zr, which were from the IL and ZrO_2, respectively. The STEM and element mapping images show that C is mainly distributed on the internal surface of the hollow ZrO_2 nanoparticles. The cross sectional compositional line profiles for the single IL@ZrO_2 nanoparticle demonstrate a coincident conclusion with the spectral element mapping (Fig. 1j). The loading amount of IL

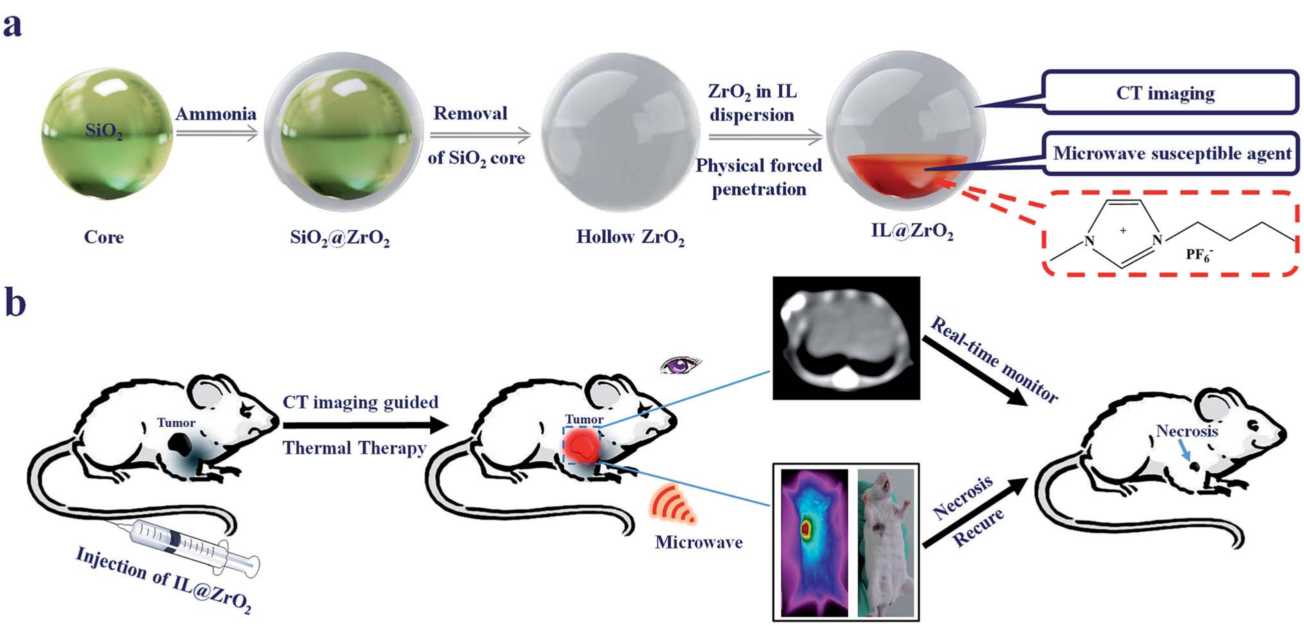

Scheme 1 (a) Schematic illustration of synthesizing hollow ZrO_2 nanoparticles *via* the template method and encapsulating IL *via* the physical forced penetration method. (b) Schematic illustration of IL@ZrO_2 as a multifunctional theranostic agent for CT imaging guided microwave thermal therapy *in vivo* and real-time monitoring of the therapeutic outcomes visually.

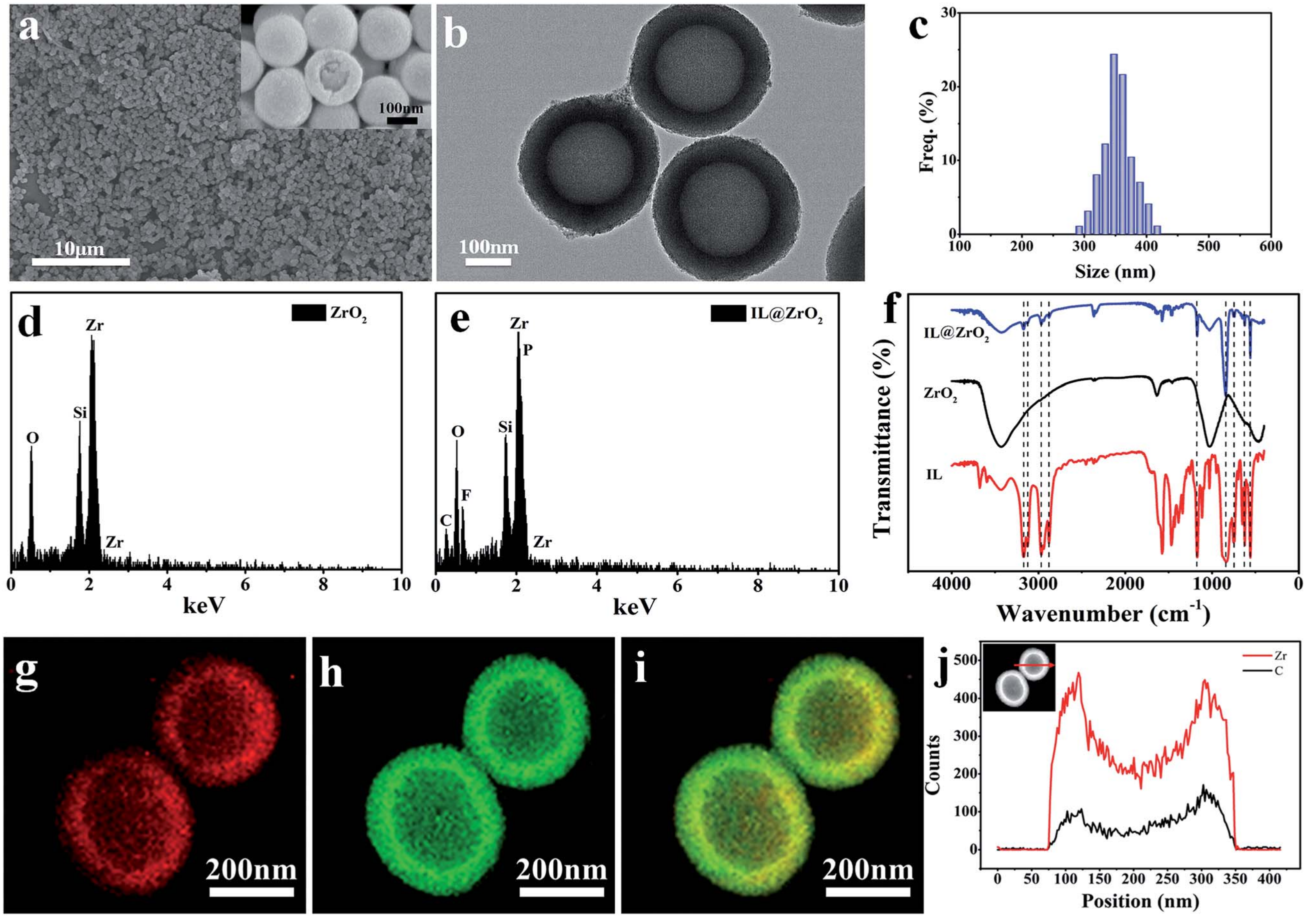

Fig. 1 Characterization of the physicochemical properties of the multifunctional IL@ZrO_2 nanoparticles. (a) Low (×5k) and high (×100k, inset) magnification SEM images, (b) TEM image, and (c) histogram of the distribution of diameters of the IL@ZrO_2 nanoparticles. The histogram of the distribution of diameters was based on statistical analysis of the results *via* measuring the size of 100 nanoparticles in (a). EDX spectra of (d) the hollow ZrO_2 nanoparticles and (e) the multifunctional IL@ZrO_2 nanoparticles. (f) FT-IR spectra of the ZrO_2 nanoparticles, multifunctional IL@ZrO_2 nanoparticles and IL. STEM-EDX spectral element mapping for (g) carbon and (h) zirconium. (i) Merged overlay image formed from (g) and (h), showing the clear structure. (j) Cross sectional compositional line profiles of IL@ZrO_2.

can be calculated *via* the TGA curves of ZrO_2 and IL@ZrO_2 (Fig. S1†). The total weight losses were 85.81% and 68.96% for ZrO_2 and IL@ZrO_2, respectively. The difference between the two values was caused by the loading of IL inside the ZrO_2 nanoparticles. Through comparing the *D*-values of the total weight losses of ZrO_2 and IL@ZrO_2, the loading amount of IL was calculated with the value of 16.85% (Fig. S1†). The selection of a hydrophobic IL can avoid leakage out of the ZrO_2 shell when dispersed in PBS solution, which results in stable microwave response properties of the IL@ZrO_2 nanoparticles.

Microwave heating *in vitro*

We first performed a microwave heating test *in vitro* to investigate the response properties of the IL@ZrO_2 nanoparticles to microwave irradiation. When irradiated by microwaves (1.8 W, 450 MHz) for 5 minutes, the temperature of the IL@ZrO_2 group rose from 30 to 58 °C, with an especially high heating rate during the first 60 s, while the temperature of the control group containing an isometric saline solution only rose to 45 °C with a relatively low heating rate. To discuss the influence of pure ZrO_2 without any IL loaded, ZrO_2 nanoparticles were used as another control group under the same microwave conditions, and poor temperature rise performance was observed (Fig. 2a). The rapidly alternating microwave field results in a change of the direction of ionic polarization, which causes frequency-dependent friction between ions, and the temperature rises. The microwave heating process can be clearly observed in the corresponding FLIR images (Fig. 2b). Significantly, the high-temperature region is gradually enlarged with prolonged microwave irradiation time, yet the temperature in the control group and ZrO_2 group only reaches about 45 °C. This demonstrates that the IL@ZrO_2 nanoparticles are suitable for microwave tumor thermotherapy.

In vitro and *in vivo* systematic toxicity evaluation results

A hemolysis test and MTT assay were primarily performed to evaluate the potential toxicity of the IL@ZrO_2 nanoparticles. Each concentration group exhibits dramatic non-hemolysis behavior, and the maximum hemolysis ratio is only 2.18% when the concentration increases to 5000 μg mL^{-1} (Fig. S2a†). The

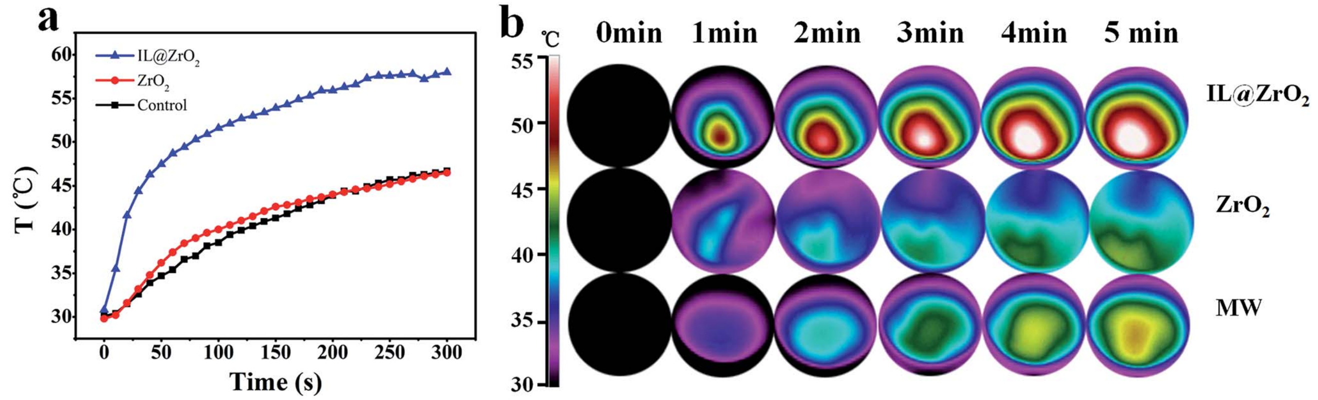

Fig. 2 Evaluation of the microwave sensitizing properties of the IL@ZrO_2 nanoparticles. (a) Heating curves of the ZrO_2 and IL@ZrO_2 nanoparticles dispersed in saline solution (1 mL, 20 mg mL^{-1}) and irradiated by microwaves (1.8 W, 450 MHz) for 5 minutes. The control group represents isometric saline solution. The temperature was recorded every 10 s with an optical fiber probe. (b) The corresponding FLIR images of the ZrO_2, IL@ZrO_2 and control groups based on (a). The pictures were taken every 1 minute.

inset picture in Fig. S2a† shows consistent visual results, with non-hemolysis for each concentration except for the positive control group. The MTT results in Fig. S2b† also display a low toxicity in the concentration range of 5–5000 μg mL^{-1}. The HepG2 cells all maintained a high viability of >80%. The HepG2 cells grow normally without any influence from the IL@ZrO_2 nanoparticles. The low toxicity and high response properties to microwave irradiation endow the IL@ZrO_2 nanoparticles with application potential in tumor microwave thermotherapy.

Next, systematic toxicity of the IL@ZrO_2 nanoparticles and microwave was evaluated *in vivo*. The change of body weight during the course shows no obvious weight loss (Fig. S2c†). Instead, the body weight in each group exhibits a growth tendency, indicating the low toxicity of the IL@ZrO_2 nanoparticles to ICR mice. Liver function is commonly assessed using alanine aminotransferase (ALT) and aspartate aminotransferase (AST) as biochemical markers. Compared with the control group, the activity of ALT and AST in each experimental group was within the normal ranges, indicating that the IL@ZrO_2 nanoparticles did not influence liver function. Similar results for glomerular filtration could be observed, which is commonly evaluated by blood urine nitrogen (BUN) and creatinine (CREA) (Fig. S2d†). As depicted in Fig. S3,† IL@ZrO_2 nanoparticles did not have any influence on the heart, liver, spleen, lung and kidney 16 days after injection, indicating that IL@ZrO_2 has no obvious toxic side effect on mice.

Microwave thermal therapy using H22 tumor bearing ICR mice *in vivo*

After the evaluation of the excellent response properties to microwave irradiation and low toxicity of the IL@ZrO_2 nanoparticles, a microwave thermotherapy experiment was designed using H22 tumor bearing ICR mice. Fig. 3a shows the mean temperature curves during the microwave thermotherapy procedure. Compared with the MW group and ZrO_2 + MW group, an obvious temperature rise can be observed in the IL@ZrO_2 + MW group. During 5 minutes of microwave irradiation, the final temperature in the IL@ZrO_2 + MW group rises rapidly to 55 °C, resulting in inhibition of the tumor growth. The package effect of the ZrO_2 shell can promote the frequency-dependent friction between ions, leading to temperature rise. However, the temperature in the control and ZrO_2 + MW group is too low to kill tumor cells efficiently. The FLIR images in Fig. 3b show the corresponding visible results. The enlarged high-temperature region of the tumor in the IL@ZrO_2 + MW group represents the temperature rise, while the high-temperature region (nearly 42 °C) in the control and ZrO_2 + MW group shows no obvious expansion.

The photos of ICR mice in Fig. 3c clearly show the therapeutic results. The tumors in the IL@ZrO_2 + MW group had disappeared after 16 days' normal feeding, while large tumors were clearly observed in other groups. The quantitative results are as shown in Fig. 3d and e. In the IL@ZrO_2 + MW group, the growth of the tumor is inhibited rapidly after the microwave treatment due to the accumulation of IL@ZrO_2 in the tumor region, while the tumors in other groups weren't inhibited, and instead grew rather rapidly (Fig. 3d). No therapeutic effects were observed in any of the control groups, suggesting that IL@ZrO_2 or microwaves alone cannot influence the growth of tumors. Only the use of IL@ZrO_2 as a microwave susceptible agent under microwave irradiation can effectively inhibit and even completely kill the tumor. Meanwhile, a slight weight increase was observed in all groups and no noticeable abnormal clinical manifestations were found, indicating the low toxicity of IL@ZrO_2 to be used as a microwave susceptible agent (Fig. 3e). The mean tumor weight of each group is shown as Fig. 3f, with the values of 0.33 ± 0.20, 2.20 ± 0.33, 2.45 ± 0.31, 2.18 ± 0.85, and 3.39 ± 0.24 g for the IL@ZrO_2 + MW, ZrO_2 + MW, IL@ZrO_2, MW and control groups, respectively. The value in the IL@ZrO_2 + MW group is significantly lower than in any control group, and the tumor inhibiting ratio was over 90%. Compared with all the control groups, there were no obvious histopathological abnormalities or lesions in the tissues (including heart, liver, spleen, lung and kidney) in the IL@ZrO_2 + MW group (Fig. S4†). The tumor cells exhibit numerous karyorrhectic debris or nuclear damage in the IL@ZrO_2 + MW group, caused by microwave hyperthermia (Fig. S5†).

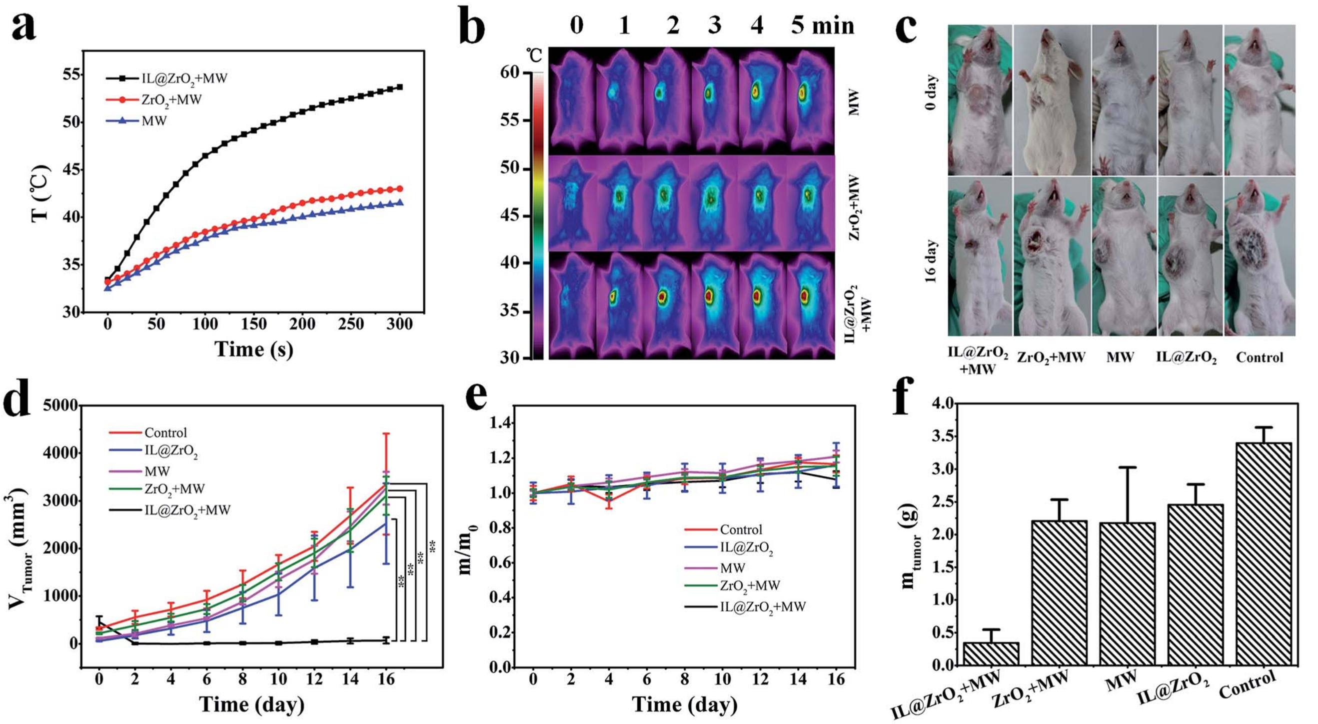

Fig. 3 Evaluation of the microwave thermal therapy efficiency of IL@ZrO$_2$ *in vivo*. (a) The mean heating curves of the tumor in the IL@ZrO$_2$ + MW, ZrO$_2$ + MW and MW groups *in vivo*, through statistical analysis of the results of five mice in each group. (b) Infrared thermal imaging pictures of ICR mice in the IL@ZrO$_2$ + MW, ZrO$_2$ + MW and MW groups, a picture of each was taken per minute. (c) Tumor volume of ICR mice in the IL@ZrO$_2$ + MW, IL@ZrO$_2$, ZrO$_2$ + MW, MW and control groups 16 days after microwave treatment. (d) Relative body weights of ICR mice in the IL@ZrO$_2$ + MW, IL@ZrO$_2$, ZrO$_2$ + MW, MW and control groups 16 days after microwave treatment. (e) Photographs of ICR mice in the IL@ZrO$_2$ + MW, IL@ZrO$_2$, ZrO$_2$ + MW, MW and control groups at 0 days and 16 days after microwave treatment. (f) Mean tumor weights of each group after excision at 16 days. (All data are presented as mean ± SD. ** denotes statistical significance for the comparison of the tumor volume in IL@ZrO$_2$ + MW group with other groups, ** $p < 0.01$).

Assessment of potential CT imaging properties of IL@ZrO$_2$ nanoparticles

CT imaging *in vitro* and *in vivo* using ICR mice bearing H22 tumor cells. CT imaging is commonly used as a kind of diagnostic tool, based on the body density dependence relationship of X-ray absorption. It is dominant over other imaging modalities due to its high-resolution and three-dimensional (3D) structural model, fast and real-time acquisition, high reproducibility, minimal injury and pain, and potential property of quantitative analysis.[9] In this paper, IL@ZrO$_2$ was employed as an ideal CT contrast agent to enhance the CT imaging quality. CT imaging *in vitro* was conducted at different concentrations (0–1.25 mg mL^{-1}) to evaluate the feasibility of IL@ZrO$_2$ as a CT contrast agent (Fig. 4a). The CT values of IL@ZrO$_2$ were significantly positively correlated with the concentration, with the color signal enhanced and tending to white based on their high atomic number and atomic mass.

Encouraged by the ideal CT imaging results *in vitro*, ICR mice bearing H22 tumor cells were used to evaluate the feasibility of IL@ZrO$_2$ as a CT contrast agent *in vivo*. IL@ZrO$_2$ was injected to the tumor site *via* subcutaneous and intravenous injection. In the both cases, the significant CT enhancement property of the tumor site was observed *via* semiquantitative and qualitative evaluation prior to and post injection (Fig. 4b and c). Quantitative analysis was further conducted *via* ICP-MS analysis of Zr in organs 12 h post intravenous injection (Fig. S6†). Zr mainly existed in the liver and spleen. The Zr content in the tumor is still relatively high and the targeting rate was over 2% ID g^{-1}. This demonstrates that IL@ZrO$_2$ has CT enhancement properties *in vivo* and can be used as an ideal CT contrast agent.

Real-time monitoring of the therapeutic outcomes visually using VXII tumor bearing SD rats. The CT imaging properties endow IL@ZrO$_2$ with potential for real-time monitoring of the therapeutic outcomes visually. VXII tumor bearing SD rats were used to preliminarily explore the feasibility. The inset of Fig. 5a represents the optical picture (left) and CT imaging picture (right) of the SD rats. As shown in the CT imaging (Fig. 5a), the growth of the tumor in the IL@ZrO$_2$ + MW group was significantly inhibited in the 5–10 days post therapy period, and even disappeared after 15 days of normal feeding, while for each control group, the tumors grew relatively rapidly. It is worth noting that the rats in each control group gradually died during days 10–15 due to cancer progression. Yet when the feeding time reached 20 days, all rats in the IL@ZrO$_2$ + MW group had normally survived without any abnormal clinical manifestations (Fig. 5b). Namely, the microwave thermotherapy can improve the survival rate of rats with ideal therapeutic efficiency (Fig. 5c). Additionally, in the groups with IL@ZrO$_2$ injection, CT signals can be observed obviously as marked in the tumor

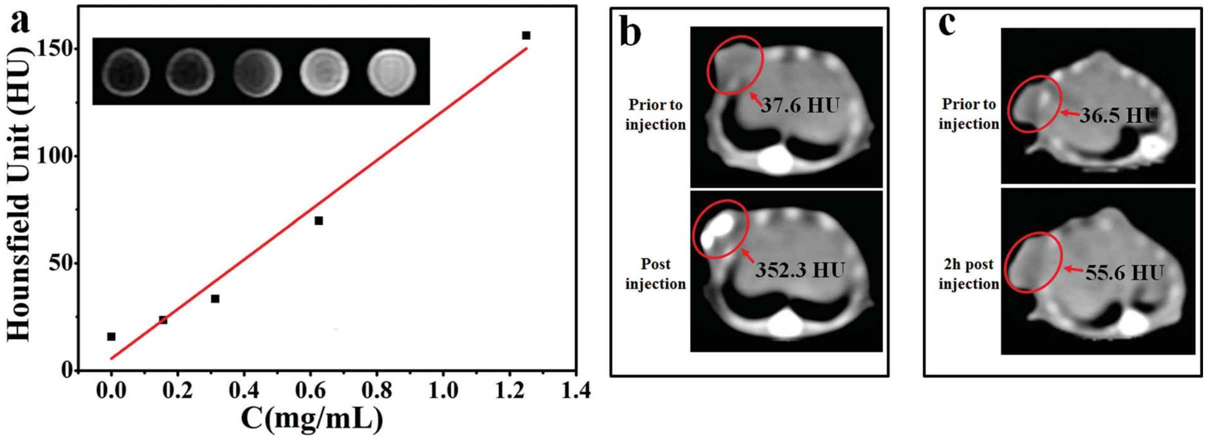

Fig. 4 CT imaging efficiency of IL@ZrO$_2$ *in vitro* and *in vivo*. (a) CT values and images (inset) of IL@ZrO$_2$ nanoparticles at different concentrations; circles from left to right in the inset represent low to high concentrations, respectively. (b) CT imaging *in vivo* prior to and post subcutaneous injection in ICR mice models. (c) CT imaging *in vivo* prior to and 2 h post intravenous injection through the mouse tail vein in ICR mice models.

region (Fig. 5a), providing proof that IL@ZrO$_2$ can be used as a CT contrast agent for real-time monitoring of the therapeutic outcomes visually.

Real-time monitoring of the biodistribution of IL@ZrO$_2$ nanoparticles in mini swine. The microwave thermotherapy efficiency in the ICR mice and SD rats *in vivo* encouraged us to next explore the potential of IL@ZrO$_2$ in a large animal model. Biodistribution of the nanomaterials *in vivo* is a key concern to evaluate the influence of nanomaterials on tissues and to discuss future clinical applications. The traditional evaluation methods focus on a single quantitative or qualitative analysis, which is difficult in monitoring the biodistribution in real-time. In addition, batches of experimental animals must be sacrificed at different times post injection to measure the biometabolic processes. Due to the CT imaging properties, the biodistribution of IL@ZrO$_2$ *in vivo* can be easily observed using a GE Lightspeed Plus. In our study, mini swine models were employed to qualitatively study the biodistribution of IL@ZrO$_2$ nanoparticles (Fig. 6). The inset of Fig. 6c represents the optical picture (left) and CT imaging picture (right) of the mini swine model. The results indicated that IL@ZrO$_2$ nanoparticles were mainly distributed in the liver, spleen and kidney at 6 h after injection. The CT value of liver and spleen reached its maximum value during 12–24 h after injection, while the CT value decreased gradually to the initial value 5 days after injection (Fig. 6a and b). The possible reason for the decrease is that the IL@ZrO$_2$ nanoparticles are biodegraded or excreted gradually from the body. For brain and muscle, the CT values show no obvious difference prior to and post injection, indicating few IL@ZrO$_2$ nanoparticles were distributed in the two tissues. The quantitative analysis was conducted *via* ICP-MS analysis of Zr in the organs. Fig. 6c shows the biodistribution of Zr in the major organs 10 days after the mini swine was sacrificed, which shows that Zr mainly existed in the spleen, lung, gallbladder, and liver. These ICP-MS results are coincident with the CT imaging results in Fig. 6b and confirm the potential application of CT imaging in real-time monitoring of the biodistribution or metabolic processes at different time points without sacrificing any experimental animals.

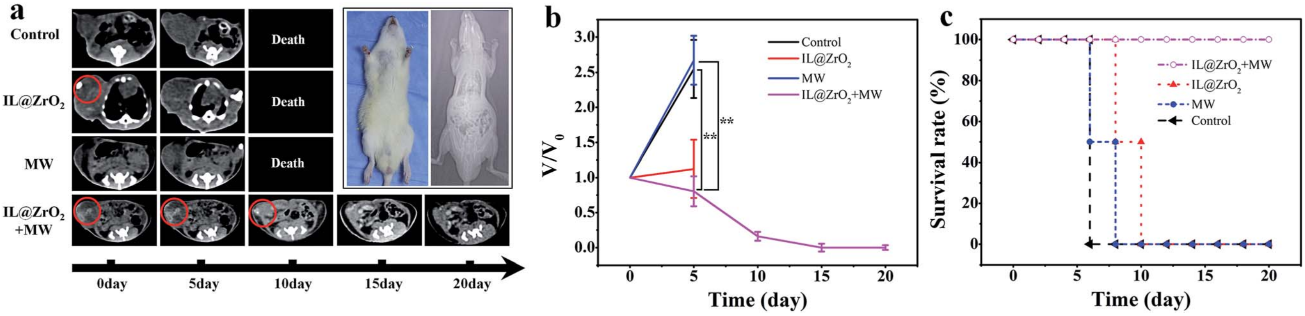

Fig. 5 Evaluation of the microwave thermal therapy efficiency of the IL@ZrO$_2$ in SD rats bearing VXII tumor cells *via* real-time CT imaging. (a) CT imaging pictures of the tumor region of each group at different time points during the thermal therapy period. The inset represents the optical picture (left) and CT imaging picture (right) of the SD rats. (b) Relative tumor volume and (c) survival rate of the SD rats in the IL@ZrO$_2$ + MW, IL@ZrO$_2$, MW and control groups at different time points after microwave treatment. The size of the tumor was measured based on the CT imaging pictures of the tumor (all data are presented as mean ± SD. ** denotes statistical significance for the comparison of the relative tumor volume in the IL@ZrO$_2$ + MW group with the MW and control groups, ** $p < 0.01$).

Hematology biochemical indicators at different time points post injection were measured to study the effect of IL@ZrO_2 nanoparticles on the blood (Fig. S7†), including white blood cell count (WBC), red blood cell count (RBC), basophile (BASO), hemoglobin (HGB), hematocrit (HCT), mean corpuscular volume (MCV), mean corpuscular hemoglobin (MCH), mean corpuscular hemoglobin concentration (MCHC), platelet count (PLT), and red cell distribution width-standard deviation (RDW-SD). None of the indicator values showed any significant difference within the normal ranges, indicating the low toxicity and excellent biocompatibility of IL@ZrO_2 nanoparticles to the mini swine.

Serum biochemical indicators at different time points post injection were measured to investigate the effect of IL@ZrO_2 nanoparticles on target organs (Fig. S8†), including alanine aminotransferase (ALT), alkaline phosphatase (ALKP), glutamyltranspetidase (GGT), total protein (TP), albumin (ALB), total bilirubin (TBIL), UREA, creatinine (CREA), lactate dehydrogenase (LDH), and C-reactive protein (CRP). None of the indicator values presented significant differences within the normal ranges, indicating low toxicity to the target organs.

A histological study of organs, including the heart, liver, spleen and lung, was performed to further investigate the effects and toxicity of IL@ZrO_2 nanoparticles. No apparent lesions or histopathological abnormalities can be observed, indicating the low toxicity of IL@ZrO_2 nanoparticles to animals (Fig. S9†). Interestingly, IL@ZrO_2 nanoparticles can be clearly observed in the liver, spleen and lung as marked in Fig. S9.† This result is coincident with the qualitative and quantitative analysis biodistribution results in Fig. 6.

Experimental section

Materials

Zirconium(IV) propoxide was purchased from Tokyo Chemical Industry Co. Ltd. 1-Butyl-3-methylimidazolium hexafluorophosphate ([Bmim]PF_6) was obtained from Shanghai Chengjie Chemical Co. Ltd. (China). 1,4-Dioxane and sodium hydroxide (NaOH) were obtained from the Beijing Chemical Reagents Company (China). Aqueous ammonia was a commercially available product. All reagents used in our work were analytical reagents (A.R.) without any further purification.

Characterization

Scanning electron microscopy (SEM, Models 4300, Hitachi) and transmission electron microscopy (TEM, JEM-2100, JEOL) were used to characterize the morphology and size distribution of ZrO_2 and IL@ZrO_2 nanoparticles. Energy dispersive X-ray spectroscopy (EDX) was used to analyze the elemental composition of ZrO_2 and IL@ZrO_2 nanoparticles. High-angle annular dark-field scanning TEM (HAADF-STEM)-energy-dispersive X-ray (EDX) (Tecnal G2 F20 U-Twin) was used to analyze the distribution of C and Zr. Fourier transform infrared spectroscopy (FT-IR, Varian, Model 3100 Excalibur) was employed to examine the composition and surface functional groups. The cell viability was measured *via* an ultraviolet and visible spectrophotometer (UV-Vis) and an enzyme-linked immunosorbent assay reader. The temperature in this work was monitored *via* an infrared thermal mapping apparatus (FLIR). Inductively coupled plasma mass spectrometry (ICP-MS) was used to quantitative analyse the biodistribution of IL@ZrO_2

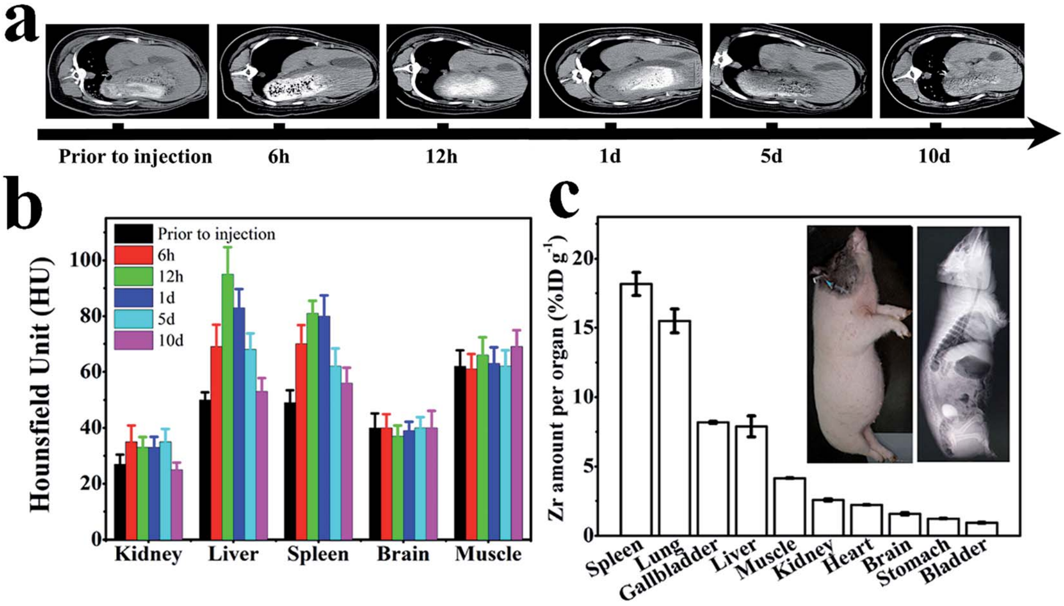

Fig. 6 Evaluation of the biodistribution of IL@ZrO_2 nanoparticles in a mini swine model. (a) CT imaging pictures of the liver at different time points prior to and post injection. (b) CT values of the organs at different time points prior to and post injection, representing the biodistribution of IL@ZrO_2 in different organs. (c) ICP-MS analysis results of IL@ZrO_2 levels in tissues of the mini swine, including spleen, lung, gallbladder, liver, muscle, kidney, heart, brain, stomach and bladder. The inset represents the optical picture (left) and CT imaging picture (right) of the mini swine model.

nanoparticles in mini swine models. An optical microscope (Olympus X71, Japan) was employed to observe the paraffin sections.

Synthesis of hollow ZrO_2 nanoparticles

Hollow ZrO_2 nanoparticles were prepared *via* a template method. During the synthesis process, SiO_2 nanoparticles were employed as templates. The detailed procedure was as below. SiO_2 nanoparticles (100 mg) underwent the dewatering process prior to being dispersed in a mixture of alcohol and acetonitrile (120 mL, the volume ratio was 3 : 1). Ammonia (1.2 mL) was added to adjust the pH value to weakly alkaline. The zirconium (Zr) precursor (0.5 mL) was then swiftly injected into the mixture under magnetic stirring. The hydrolytic process of Zr was triggered in the weakly alkaline environment to induce the growth of small ZrO_2 nanoparticles with SiO_2 as seeds. As the reaction proceeded for 6 h, a ZrO_2 shell was formed gradually on the surface of the SiO_2 seed. The thickness of the shell can be controlled through adjusting the ratio of the Zr precursor and the SiO_2 seeds and the reaction time. To remove the SiO_2 seed core, NaOH solution (1 mL, 1 M) was added under a temperature of 80 °C for approximately 4 h. The obtained hollow ZrO_2 nanoparticles were collected by centrifugation and washed three times with deionized water (Scheme 1a).

Preparation of multifunctional IL@ZrO_2 nanoparticles *via* a novel physical forced penetration method

A hydrophobic IL, 1-butyl-3-methylimidazolium hexafluorophosphate ([Bmim]PF_6), was selected as a microwave susceptible agent to be encapsulated into the as-prepared hollow ZrO_2 nanoparticles *via* a novel and simple physical forced penetration method. [Bmim]PF_6 (0.5 mL) was dispersed in 1,4-dioxane (5 mL), followed by dispersion in alcohol (5 mL) under ultrasonication. The as-prepared hollow ZrO_2 nanoparticles (20 mg) were then added into the solution. The reaction system was kept under vacuum condition with a water pump under continuous ultrasonication for 30 minutes. The IL could gradually diffuse into the hollow structure through the thin ZrO_2 shell, due to the concentration difference and physical pressure. As time continued, multifunctional IL@ZrO_2 nanoparticles were obtained and washed three times with deionized water (Scheme 1a).

Microwave heating experiment *in vitro*

A microwave heating experiment *in vitro* was designed to evaluate the microwave susceptibility properties of the IL@ZrO_2 nanoparticles. 1 mL IL@ZrO_2 or ZrO_2 dispersions (20 mg mL^{-1} in saline solution) were added into the reactor and then irradiated by microwaves (1.8 W, 450 MHz) for 5 minutes. The control group contained isometric saline solution. During the microwave irradiation process, the temperature values were recorded every 10 s with an optical fiber probe. To visually monitor the temperature change, real-time thermal imaging was monitored with FLIR, which corresponded well with the optical fiber probe results.

Hemolysis test

A hemolysis test was necessary to preliminarily estimate the potential toxicity of the IL@ZrO_2 nanoparticles. Rabbit's heart blood was employed to prepare red blood cell dispersions in PBS solution (2 v%). 0.5 mL cell dispersion was mixed with isometric IL@ZrO_2 PBS solutions with a wide concentration range (5–5000 μg mL^{-1}). The positive and negative control groups were designed to replace IL@ZrO_2 dispersions with isometric deionized water and PBS solution, respectively. Each group contained three parallel experiments in duplicate to minimize statistical error. After a 3 h incubation period, these mixtures were centrifuged and UV-Vis was used to measure the absorbance of the supernatant at 570 nm.

Cell culture and animal model

All animal experiments in our work were performed in compliance with the Institutional Animal Care and Use Committee of Technical Institute of Physics and Chemistry, Chinese Academy of Sciences and First Hospital of China Medical University, China. Human liver carcinoma cells, HepG2 cell line (purchased from ATCC), were cultured in a high-glucose DMEM medium at 37 °C with 5% CO_2 in a humid atmosphere. Six-week-old ICR female mice weighing 20–25 g (provided by Vital River Laboratory Animal Technology Co. Ltd.) were subcutaneously implanted with $2–3 \times 10^6$ H22 tumor cells in the left anterior axillary. The CT imaging and microwave thermal therapy experiments *in vivo* were performed after the tumor volume reached about 100 mm^3. The acute toxicity test *in vivo* was performed with healthy six-week-old ICR female mice without tumor cells implanted.

MTT assay

A MTT assay was conducted to evaluate the potential cytotoxicity of the IL@ZrO_2 nanoparticles. A 96-well plate seeded with 100 μL HepG2 cells in each well (around 10 000 cells) was incubated overnight in culture conditions to allow for the cell attachment. Subsequently, to each well was added 100 μL IL@ZrO_2 dispersed in the culture medium with a wide concentration range (5–5000 μg mL^{-1}). Then the 96-well plate was incubated for another 24 h in culture conditions. The control group was designed to replace the IL@ZrO_2 dispersions with isometric DMEN culture medium. 20 μL of MTT solution (3-(4,5-dimethylthiazol-2-yl)-2,5-diphenyltetrazolium bromide, final concentration was 0.5 mg mL^{-1}) was added into each well and the 96-well plate was incubated for another 4 h in culture conditions. The growth medium was removed and the cells were washed three times with PBS solution. The absorbance of each well was measured at 492 nm on an enzyme-linked immunosorbent assay reader. The cell viability (%) = 100 X optical density (OD) of experimental group/OD of control group. Each group contained five parallel experiments in duplicate.

Systematic toxicity testing *in vivo*

Systematic toxicity testing *in vivo via* intravenous injection was needed and a typical procedure was designed as below. Healthy female ICR mice were divided into five groups ($n = 3$ in each group), including a control (without any treatment), IL@ZrO$_2$ (only IL@ZrO$_2$ added without microwave treatment), ZrO$_2$ (ZrO$_2$ added without microwave treatment) MW (only microwave treated without IL@ZrO$_2$ added) and IL@ZrO$_2$ + MW (combined microwave treatment with IL@ZrO$_2$ added) groups. The nanoparticles were injected *via* intravenous injections through the mouse tail vein and the dose for each group was 40 mg mL^{-1}. Twelve hours after injection, the IL@ZrO$_2$ + MW and MW groups were irradiated by microwaves (1.8 W, 450 MHz) for 5 minutes, in correspondence with the thermal therapy experiment. The clinical manifestation of the mice was observed and their weight was recorded carefully throughout the experiment period. The mice were sacrificed after 16 days' normal feeding. Simultaneously, a venous blood sample was collected for blood biochemistry examination, including alanine aminotransferase (ALT), aspartate aminotransferase (AST), blood urea nitrogen (BUN), and creatinine (CREA). The tissues and organs, including the liver, spleen, lung, and kidney, were excised and fixed in formalin solution (10%) for further histological study.

Tumor microwave thermal therapy experiment using ICR mice bearing H22 tumor cells

After optimization of the therapeutic conditions, an injection dose of 40 mg kg^{-1} and 1.8 W, 450 MHz microwave irradiation for 5 minutes were used for the tumor thermal therapy *in vivo*. Six-week-old ICR female mice (20–25 g) bearing H22 tumors were used for the tumor microwave thermal therapy experiment. The mice were divided into the following five groups ($n = 5$ in each group): control (without any treatment), IL@ZrO$_2$ (only IL@ZrO$_2$ added without microwave treatment, the injected dose was 40 mg kg^{-1}), MW (only microwave treated without IL@ZrO$_2$ added), ZrO$_2$ + MW (combined microwave treatment with ZrO$_2$ added, the injected dose was 40 mg kg^{-1}) and IL@ZrO$_2$ + MW (combined microwave treatment with IL@ZrO$_2$ added, the injected dose was 40 mg kg^{-1}). The IL@ZrO$_2$ and ZrO$_2$ were injected *via* the intravenous injection method through the mouse tail vein and the microwave treatment (1.8 W, 450 MHz) was given 12 h after injection, so that an abundant amount of nanoparticles could be targeted to the tumor region (Scheme 1b). The microwave irradiation time was set for 5 minutes and the temperature values were recorded every 10 s with an optical fiber probe. To visually monitor the temperature change of the tumor region, real-time thermal imaging was monitored with FLIR. During our experiments, anesthesia was maintained using pentobarbital sodium (2 w%, 0.2 mL). Each group was designed to contain three parallel mice. After treatment, the tumor volume and body weight were monitored every two days and tumor volume can be calculated through formula (1). The tumor volume and relative body weight were calculated to make the results more understandable. The mice were sacrificed after 16 days' normal feeding and the tissues and organs, including liver, spleen, lung, and kidney, were excised and fixed in formalin solution (10%) for further histological study.

$$V_{\text{tumor}} = \frac{ab^2}{2} \tag{1}$$

where a and b refer to the length and width of tumor, respectively.

CT imaging experiments

CT imaging *in vitro*. CT imaging *in vitro* was performed using a GE Lightspeed Plus. Isometric IL@ZrO$_2$ dispersed in PBS solutions with a wide concentration range (1.25, 0.65, 0.30, 0.15, 0 mg mL^{-1}) was added into a PE tube and then scanned with the GE Lightspeed Plus. The group containing pure PBS solution was designed as the control group. The CT value of each group was recorded to evaluate the CT contrast properties of the IL@ZrO$_2$ nanoparticles.

CT imaging of H22 tumor bearing ICR mice *in vivo*. CT imaging of H22-bearing ICR mice *in vivo* was performed using a Philips Brilliance iCT256, and the mice were scanned prior to and 2 h post injection of IL@ZrO$_2$ with the dose of 40 mg kg^{-1} (Scheme 1b). The different CT values in the tumor region prior to and post injection of IL@ZrO$_2$ confirmed the ideal CT imaging application *in vivo*. The injection was achieved *via* subcutaneous and intravenous injection to explore the feasibility of IL@ZrO$_2$ as a CT contrast agent *in vivo*.

Real-time monitoring of the therapeutic outcomes visually using SD rats bearing VXII tumor cells. SD rats (200 g) bearing VXII tumor cells were employed to further explore the potential application of IL@ZrO$_2$. The experiment procedure was similar to the ICR mice experiment. SD rats were divided into four groups, control (without any treatment), IL@ZrO$_2$ (only IL@ZrO$_2$ added without microwave treatment, the injected dose was 80 mg kg^{-1}), MW (only microwave treated without IL@ZrO$_2$ added), and IL@ZrO$_2$ + MW (combined microwave treatment with IL@ZrO$_2$ added, the injected dose was 80 mg kg^{-1}). The IL@ZrO$_2$ was injected to tumor sites *via* subcutaneous injection and microwaves (1.8 W, 450 MHz) were applied for 5 minutes. CT imaging was performed at different time points post microwave therapy to monitor the change in the tumors. Tumor volume was measured from the CT imaging and calculated through formula (1). Relative tumor volume was calculated to make the results more understandable.

Real-time monitoring of the biodistribution of IL@ZrO$_2$ nanoparticles in the mini swine model. All experiments performed on mini swine models were approved by the Institutional Animal Care. Healthy mini swine weighing 50 kg were used for the study of the biodistribution of IL@ZrO$_2$ nanoparticles. IL@ZrO$_2$ nanoparticles were injected intravenously with a dose of 6 mg kg^{-1}. CT imaging and inductively coupled plasma atomic emission spectroscopy (ICP-MS) were employed to conduct the qualitative and quantitative analysis at different times post injection, respectively. Meanwhile, blood was collected for hematology and serum biochemistry analysis. The mini swine were sacrificed 10 days post injection and the organs were collected for subsequent ICP-MS analysis and histological study.

Histological study

A typical histological study was conducted using standard laboratory procedures. The tissues were fixed in formalin solution (10%) for 24 h and the deprivation process of body fluids was followed. Subsequently, the tissues were embedded in paraffin blocks and sectioned into thin paraffin sections (5 μm in thickness). To identify the cell and organization structure, the paraffin sections were then stained with hematoxylin and eosin (H&E stain) and observed using an optical microscope (Olympus X71, Japan).

Statistical analysis

All experimental results were performed as mean ± standard deviation (S.D). Multigroup comparisons of the data were carried out using a one-way analysis of variance (ANOVA) test using SPSS Statistics 17.0. The level of significance for all tests was set at $p < 0.05$.

Conclusions

We introduced a simple IL@ZrO_2 nanostructure *via* a physical forced penetration method. The ZrO_2 shell produces an enhanced CT imaging effect which allows highly sensitive detection *in vivo* and *in vitro*, and the IL inside produces a microwave susceptibility effect which allows excellent thermotherapy efficiency. Namely, the simple nanostructure can be used as a multifunctional theranostic agent for CT imaging guided microwave thermal therapy. Upon microwave irradiation, the tumor inhibiting ratio was over 90% in H22 tumor bearing ICR mice. In addition, we demonstrated the biodistribution of IL@ZrO_2 in the tissues of a mini swine model through CT imaging and ICP-MS analysis with coincident results, providing valuable proof of the potential CT imaging *in vivo*. This versatility of the CT imaging and microwave susceptibility properties endows the multifunctional nanoparticles with the ability to be a useful platform for imaging guided therapy of tumors and real-time monitoring of the biodistribution and metabolic processes or assessment of therapeutic outcomes visually.

Acknowledgements

The authors acknowledge financial support from the National Hi-Technology Research and Development Program (863 Program) (no. 2012AA022701 and 2013AA032201), the National Natural Science Foundation of China (NSFC) (no. 61171049, 51202260, 81201814, 31400854, 31271075, and 31270022).

Notes and references

1 Y. Li, T. Y. Lin, Y. Luo, Q. Liu, W. Xiao, W. Guo, D. Lac, H. Zhang, C. Feng, S. Wachsmann-Hogiu, J. H. Walton, S. R. Cherry, D. J. Rowland, D. Kukis, C. Pan and K. S. Lam, *Nat. Commun.*, 2014, **5**, 4712.

2 Z. Zha, J. Wang, E. Qu, S. Zhang, Y. Jin, S. Wang and Z. Dai, *Sci. Rep.*, 2013, **3**, 2360.

3 L. Cheng, J. Liu, X. Gu, H. Gong, X. Shi, T. Liu, C. Wang, X. Wang, G. Liu, H. Xing, W. Bu, B. Sun and Z. Liu, *Adv. Mater.*, 2014, **26**, 1886.

4 H. Ke, J. Wang, Z. Dai, Y. Jin, E. Qu, Z. Xing, C. Guo, X. Yue and J. Liu, *Angew. Chem., Int. Ed.*, 2011, **50**, 3017.

5 A. Gianella, P. A. Jarzyna, V. Mani, S. Ramachandran, C. Calcagno, J. Tang, B. Kann, W. J. R. Dijk, V. L. Thijssen, A. Griffioen, G. Storm, Z. A. Fayad and W. J. M. Mulder, *ACS Nano*, 2011, **5**, 4422.

6 L. S. Lin, Z. X. Cong, J. B. Cao, K. M. Ke, Q. L. Peng, J. Gao, H. H. Yang, G. Liu and X. Chen, *ACS Nano*, 2014, **8**, 3876.

7 T. D. MacDonald, T. W. Liu and G. Zheng, *Angew. Chem., Int. Ed.*, 2014, **53**, 6956.

8 W. Fan, B. Shen, W. Bu, F. Chen, Q. He, K. Zhao, S. Zhang, L. Zhou, W. Peng, Q. Xiao, D. Ni, J. Liu and J. Shi, *Biomaterials*, 2014, **35**, 8992.

9 H. Xing, X. Zheng, Q. Ren, W. Bu, W. Ge, Q. Xiao, S. Zhang, C. Wei, H. Qu, Z. Wang, Y. Hua, L. Zhou, W. Peng, K. Zhao and J. Shi, *Sci. Rep.*, 2013, **3**, 1751.

10 H. Shi, X. Ye, X. He, K. Wang, W. Cui, D. He, D. Li and X. Jia, *Nanoscale*, 2014, **6**, 8754.

11 R. Schoffelen, O. C. Boerman, D. M. Goldenberg, R. M. Sharkey, C. M. van Herpen, G. M. Franssen, W. J. McBride, C. H. Chang, E. A. Rossi, W. T. van der Graaf and W. J. Oyen, *Br. J. Cancer*, 2013, **109**, 934.

12 H. Liu, D. Chen, L. Li, T. Liu, L. Tan, X. Wu and F. Tang, *Angew. Chem., Int. Ed.*, 2011, **50**, 891.

13 Y. W. Won, S. M. Yoon, K. S. Lim and Y. H. Kim, *Adv. Funct. Mater.*, 2012, **22**, 1199.

14 T. J. Li, C. C. Huang, P. W. Ruan, K. Y. Chuang, K. J. Huang, D. B. Shieh and C. S. Yeh, *Biomaterials*, 2013, **34**, 7873.

15 M. H. Oh, N. Lee, H. Kim, S. P. Park, Y. Piao, J. Lee, S. W. Jun, W. K. Moon, S. H. Choi and T. Hyeon, *J. Am. Chem. Soc.*, 2011, **133**, 5508.

16 Y. C. Tseng, Z. Xu, K. Guley, H. Yuan and L. Huang, *Biomaterials*, 2014, **35**, 4688.

17 Y. Wu, Y. Sun, X. Zhu, Q. Liu, T. Cao, J. Peng, Y. Yang, W. Feng and F. Li, *Biomaterials*, 2014, **35**, 4699.

18 H. Hong, K. Yang, Y. Zhang, J. Engle, L. Feng, Y. Yang, T. R. Nayak, S. Goel, J. Bean, C. P. Theuer, T. E. Barnhart, Z. Liu and W. Cai, *ACS Nano*, 2012, **6**, 2361.

19 F. Chen, H. Hong, Y. Zhang, H. F. Valdovinos, S. Shi, G. S. Kwon, C. P. Theuer, T. E. Barnhart and W. Cai, *ACS Nano*, 2013, **7**, 9027.

20 L. Jing, X. Liang, Z. Deng, S. Feng, X. Li, M. Huang, C. Li and Z. Dai, *Biomaterials*, 2014, **35**, 5814.

21 Z. Sheng, L. Song, J. Zheng, D. Hu, M. He, M. Zheng, G. Gao, P. Gong, P. Zhang, Y. Ma and L. Cai, *Biomaterials*, 2013, **34**, 5236.

22 F. Chen, W. Bu, S. Zhang, J. Liu, W. Fan, L. Zhou, W. Peng and J. Shi, *Adv. Funct. Mater.*, 2013, **23**, 298.

23 S. Zeng, Z. Yi, W. Lu, C. Qian, H. Wang, L. Rao, T. Zeng, H. Liu, H. Liu, B. Fei and J. Hao, *Adv. Funct. Mater.*, 2014, **24**, 4051.

24 V. P. Chauhan, J. D. Martin, H. Liu, D. A. Lacorre, S. R. Jain, S. V. Kozin, T. Stylianopoulos, A. S. Mousa, X. Han, P. Adstamongkonkul, Z. Popovic, P. Huang,

M. G. Bawendi, Y. Boucher and R. K. Jain, *Nat. Commun.*, 2013, **4**, 2516.

25 J. Li, L. S. Lindstrom, J. N. Foo, S. Rafiq, M. K. Schmidt, P. D. Pharoah, K. Michailidou, J. Dennis, M. K. Bolla, Q. Wang, L. J. Van't Veer, S. Cornelissen, E. Rutgers, M. C. Southey, C. Apicella, G. S. Dite, J. L. Hopper, P. A. Fasching, L. Haeberle, A. B. Ekici, M. W. Beckmann, C. Blomqvist, T. A. Muranen, K. Aittomaki, A. Lindblom, S. Margolin, A. Mannermaa, V. M. Kosma, J. M. Hartikainen, V. Kataja, G. Chenevix-Trench, I. K. Con Fab, K. A. Phillips, S. A. McLachlan, D. Lambrechts, B. Thienpont, A. Smeets, H. Wildiers, J. Chang-Claude, D. Flesch-Janys, P. Seibold, A. Rudolph, G. G. Giles, L. Baglietto, G. Severi, C. A. Haiman, B. E. Henderson, F. Schumacher, L. Le Marchand, V. Kristensen, G. I. Alnaes, A. L. Borresen-Dale, S. Nord, R. Winqvist, K. Pylkas, A. Jukkola-Vuorinen, M. Grip, I. L. Andrulis, J. A. Knight, G. Glendon, S. Tchatchou, P. Devilee, R. Tollenaar, C. Seynaeve, M. Hooning, M. Kriege, A. Hollestelle, A. van den Ouweland, Y. Li, U. Hamann, D. Torres, H. U. Ulmer, T. Rudiger, C. Y. Shen, C. N. Hsiung, P. E. Wu, S. T. Chen, S. H. Teo, N. A. Taib, C. Har Yip, G. Fuang Ho, K. Matsuo, H. Ito, H. Iwata, K. Tajima, D. Kang, J. Y. Choi, S. K. Park, K. Y. Yoo, T. Maishman, W. J. Tapper, A. Dunning, M. Shah, R. Luben, J. Brown, C. C. Khor, D. M. Eccles, H. Nevanlinna, D. Easton, K. Humphreys, J. Liu, P. Hall and K. Czene, *Nat. Commun.*, 2014, **5**, 4051.

26 J. P. Dassie, L. I. Hernandez, G. S. Thomas, M. E. Long, W. M. Rockey, C. A. Howell, Y. Chen, F. J. Hernandez, X. Y. Liu, M. E. Wilson, L. A. Allen, D. A. Vaena, D. K. Meyerholz and P. H. Giangrande, *Mol. Ther.*, 2014, **22**, 1910.

27 M. Di Matteo, E. Samara-Kuko, N. J. Ward, S. N. Waddingon, J. H. McVey, M. K. Chuah and T. VandenDriessche, *Mol. Ther.*, 2014, **22**, 1614.

28 V. Biju, *Chem. Soc. Rev.*, 2014, **43**, 744.

29 C. Ratanatawanate, A. Chyao and K. J. Balkus Jr, *J. Am. Chem. Soc.*, 2011, **133**, 3492.

30 X. Wang, H. Liu, D. Chen, X. Meng, T. Liu, C. Fu, N. Hao, Y. Zhang, X. Wu, J. Ren and F. Tang, *ACS Appl. Mater. Interfaces*, 2013, **5**, 4966.

31 A. K. Rengan, M. Jagtap, A. De, R. Banerjee and R. Srivastava, *Nanoscale*, 2014, **6**, 916.

32 W. J. Smith, N. P. Oien, R. M. Hughes, C. M. Marvin, Z. L. Rodgers, J. Lee and D. S. Lawrence, *Angew. Chem., Int. Ed.*, 2014, **53**, 10945.

33 H. Shi, T. Liu, C. Fu, L. Li, L. Tan, J. Wang, X. Ren, J. Ren, J. Wang and X. Meng, *Biomaterials*, 2015, **44**, 91.

34 Q. Du, C. Fu, J. Tie, T. Liu, L. Li, X. Ren, Z. Huang, H. Liu, F. Tang, L. Li and X. Meng, *Nanoscale*, 2015, **7**, 3147.

35 N. E. Leadbeater and H. M. Torenius, *J. Org. Chem.*, 2002, **67**, 3145.

36 C. Fu, T. Liu, L. Li, H. Liu, D. Chen and F. Tang, *Biomaterials*, 2013, **34**, 2565.

37 T. Liu, L. Li, C. Fu, H. Liu, D. Chen and F. Tang, *Biomaterials*, 2012, **33**, 2399.

38 F. Devun, J. Biau, M. Huerre, A. Croset, J. S. Sun, A. Denys and M. Dutreix, *Radiology*, 2014, **270**, 736.